Journal of Magnetism and Magnetic Materials 581 (2023) 170980

Contents lists available at ScienceDirect

Journal of Magnetism and Magnetic Materials

journal homepage: www.elsevier.com/locate/jmmm

Investigation of structural, elastic and magnetic properties of Cu^{2+} ions substituted cobalt nano ferrites

Atul Thakur [a,b,c,d,*], Ritesh Verma [c,d,e], Fayu Wan [a], Blaise Ravelo [a], Irina Edelman [f], Sergei Ovchinnikov [e], Preeti Thakur [c,d,*]

[a] School of Electronics and Information Engineering, Nanjing University of Information Science & Technology, Nanjing 210044, China
[b] NanoLatticeX, Amity University Haryana, Gurugram, Haryana 122413, India
[c] Nanotechnology Wing, Innovative Science Research Society, Shimla 177002, India
[d] Centre for Nanotechnology, Amity University Haryana, Gurugram 122413, India
[e] Department of Physics, Amity University Haryana, Gurugram 122413, India
[f] Kirensky Institute of Physics, Federal Research Center KSC, Siberian Branch, Russian Academy of Sciences, 50 Akademgorodok, Krasnoyarsk 660036, Russia

ARTICLE INFO

Keywords:
Nanoferrites
Structure
Rietveld Refinement
Elastic Properties
Magnetic Porperties

ABSTRACT

In the present work, we synthesized the Cu-doped $CoFe_2O_4$ ($Co_{1-x}Cu_xFe_2O_4$) nanoparticles with × = 0.0, 0.2, 0.4 and 0.6, by employing the citrate precursor method. The X-ray Diffraction (XRD) pattern confirmed the pure cubic structure formation with the *Fd-3m* space group. To know the structural purity of each sample as well as the distribution of cations, Rietveld refinement was carried out. The crystallite size increases from 39.55 nm to 41.80 nm upto x = 0.2 and with further doping of Cu^{2+} ions it decreases to 36.27 nm. Similar variation is observed in the lattice parameter where the value of '*a*' first increases from 8.378 Å to 8.381 Å and then decreases to 8.377 Å. The development of a non-uniform grain is seen using scanning electron microscope (SEM), which reveals the reduction in grain size. Fourier Transform Infrared Spectroscopy (FTIR) showed the two peaks ν_1 and ν_2 for all the samples around 541 cm^{-1} and 408 cm^{-1}, respectively, which further decreases to 532.5 cm^{-1} and 402.5 cm^{-1} as the dopant ion concentration increases. The Stiffness constant, and Elastic modulus decrease with doping whereas, the Poisson's ratio and Pugh's ratio show a constant value of around 0.249 and 1.660, respectively. Vibrating Sample Magnetometer (VSM) analysis shows a decrease in saturation magnetization (σ_s) value from 76.85 emu/g to 43.62 emu/g. The net magnetic moment (n_B) decreases from 3.29 μ_B to 1.85 μ_B and the effective anisotropy constant value decreases from 10.672erg/g to 4.461erg/g. Thus, the prepared nanoparticles provide a way forward for their industrial applications.

1. Introduction

Due to their superior magnetic properties, spinel nano-ferrites have generated a great deal of interest for their potential use as high-density data storage, magnetic switches, delivery of drugs, magnetically charged fluids, high-power magnets, catalysis, and microwave absorbers [1–5]. The advanced applications of spinel nano ferrites are because in the nano dimension, particles show extraordinary behaviour as compared to their bulk counterpart. It is observed that most of the applications of spinel nanoferrites arise due to their strong dependency on magnetic characteristics, whereas, the magnetic traits depend on the cation distribution and spin canting effect [6,7].

Cobalt ferrite ($CoFe_2O_4$) is a material that is widely recognized for a variety of applications, making it stand out among the other spinel ferrites that are known. In the bulk compound of $CoFe_2O_4$, the structure is an inverse spinel. This means that the Fe^{3+} ions are evenly distributed between the tetrahedral (A) site and the octahedral (B) sites, while the Co^{2+} ions more preferentially occupy the octahedral site. $CoFe_2O_4$ nanoferrites, on the other hand, have numerous applications in ferrofluid technology, cancer treatment, magnetic resonance imaging (MRI), and microwave devices due to their mechanical stiffness, chemical stability, high anisotropy as $K_a = 3 \times 10^5$ J/m^3, and high value of saturation magnetization and the coercivity [8–12]. Their physical characteristics are determined by numerous factors, including the technique of

* Corresponding authors at: Centre for Nanotechnology, Amity University Haryana, Gurugram- 122413, India (Preeti Thakur); Nanijing University of Information Science & Technology, Nanjing 210044, China (Atul Thakur).
E-mail addresses: 100108@nuist.edu.cn (A. Thakur), pthakur@ggn.amity.edu (P. Thakur).

https://doi.org/10.1016/j.jmmm.2023.170980
Received 6 June 2023; Received in revised form 22 June 2023; Accepted 26 June 2023
Available online 1 July 2023

manufacture, the chemical composition, the sintering temperature, and the distribution of cations. On the other hand, the low sensitivity of the $CoFe_2O_4$ nanoparticles to strain is due to the high anisotropy of the material.

To improve the mechanical stability and magnetic properties of $CoFe_2O_4$ nanoparticles, one of the finest ways is to substitute them with suitable ions with large or similar ionic radii. Thus, the substitution of $CoFe_2O_4$ nano ferrites with suitable atoms or ions can significantly improve their structural, mechanical and magnetic properties which can readily make them a preferential candidate for biomedical drug delivery applications, switching and memory devices, microwave devices, electromagnetic interference shielding applications etc. [13,14]. Several studies have been reported on the substitution of $CoFe_2O_4$ nanoparticles with suitable ions in order to improve their physical properties. *Balavijayalakshmi et al.,* studied the influence of copper doping on cobalt ferrite nanoparticles [12]. It was observed that the magnetic parameters such as coercivity, remnant magnetization and saturation magnetization decrease with an increase in copper ions concentration. The magnetic parameters decreased because copper doping increased the net magnetization at B site which in turn decreased the net magnetization. Similarly, *Mohamed et al.,* again synthesized Cu^{2+} ions doped cobalt ferrite nanoparticles in order to investigate the effect of doping on their structural, optical and magnetic characteristics [15]. With doping, the optical energy gap ranged between 1.77 eV and 2.20 eV due to which the nanoparticles were assumed to be a good candidate for water purification. The saturation magnetization value increased from 79 emu/g to 106 emu/g. *Aziz et al.,* substituted $CoFe_2O_4$ nanoparticles with Dysprosium (Dy^{3+}) and studied the influence of grinding methods on the structural, magnetic and morphological properties of synthesized nanoparticles [16]. The largest coercivity was found in manual-dry ground powder, whereas the ultrasonic wet ground powder showed the minimum saturation magnetization value. In another work, *Siva et al.,* doped cobalt ferrite with Mn and Cu ions and studied their magnetic and magnetostrictive properties [17]. The obtained results revealed that doping could significantly lead to the enhancement in piezomagnetic coefficient $\left(\frac{d\lambda}{dH}\right)$ of cobalt ferrite nanoparticles. As a result, the magnetic field related to the highest piezomagnetic coefficient is significantly reduced. In the latest research, *Jing et al.,* doped the cobalt ferrite nanoparticles with different rare earth (RE) ions and studied the influence of the mechanism of different substitution positions [18]. It was observed that the substitution of Co^{2+} ions by RE^{3+} ions cause a large lattice distortion and the production of smaller grains as compared to the substitution of Fe^{3+} ions by RE^{3+} ions. In addition, the results revealed that the coercivity increases significantly when Co^{2+} ions are substituted by RE^{3+} ions and decreased for the substitution of Fe^{3+} ions.

Thus, the afore-discussed literature revealed that the substitution of $CoFe_2O_4$ nanoparticles with suitable ions could significantly improve their structural, morphological, optical, mechanical and magnetic properties. In particular, copper as a dopant can readily modulate the physical and chemical properties of cobalt ferrite nanoparticles because of its comparable ionic radii, same valency and transitional nature. Keeping this information in mind, we synthesized Cu-doped $CoFe_2O_4$ ferrite nanoparticles ($Co_{1-x}Cu_xFe_2O_4$, where $\times$ = 0.0, 0.2, 0.4 and 0.6) using the citrate precursor method and the obtained ferrite nanoparticles were characterized for the structural, morphological, optical and magnetic properties.

2. Materials and methods

The Cu-doped $CoFe_2O_4$ ferrite nanoparticles, with chemical formula $Co_{1-x}Cu_xFe_2O_4$, where $\times$ = 0.0, 0.2, 0.4 and 0.6, were synthesized using the citrate precursor method [19]. In order to synthesize the pristine and doped nanoparticles, the stoichiometric amount of AR graded chemicals of Sigma Aldrich (99.9% purity), such as cobalt nitrate [$Co(NO_3)_2{\cdot}6H_2O$], copper nitrate [$Cu(NO_3)_2$], ferric nitrate [$Fe(NO_3)_3{\cdot}9H_2O$] were taken as starting precursors. The chemicals were mixed first in 200 ml deionized water on a hot plate magnetic stirrer under room temperature conditions, till a clear solution is achieved. Afterward, the stoichiometric amount of citric acid ($C_6H_8O_7{\cdot}H_2O$) was added to the mixture under constant stirring. The temperature of the hot plate was kept at 70 °C for the reaction to occur. The solution was heated for a few hours on a hot plate and after a few hours, a solid residue (loose powder) was obtained. The obtained loose powder was then crushed and calcined at 650 °C for 3 h at a heating rate of 3 °C/minute in a muffle furnace and then allowed to cool down naturally again in a muffle furnace. The prepared nanopowders were again crushed and collected for structural, morphological, optical, and magnetic characterizations. Fig. 1 shows the diagram of the procedure.

3. Characterization techniques

In order to determine the phase and structure of the sample at ambient temperature, a Japanese X-ray diffractometer of Ringaku Minifiex 600 was used in combination with CuK radiation with a wavelength of 1.54 Å. The scanning is carried out in the 2θ range ($20^\circ \leq 2\theta \leq 70^\circ$) at a rate of 2°/min. The surface morphology of all the samples is analyzed by using scanning electron microscopy (SEM) (Hitachi SU 8010) at an operating voltage of 15 kV. Infrared (FTIR) analysis was carried out in the range of 400 cm^{-1}–4000 cm^{-1} using a spectrometer (Perkin Elmer 400 FTIR). Using a vibrating sample magnetometer (model number Lake Shore 7305), the magnetic ordering of the synthesized ferrite nanoparticles was examined at room temperature.

4. Results and discussion

4.1. Structural and microstructural analysis

Fig. 2 shows the XRD patterns of synthesized $Cu_xCo_{1-x}Fe_2O_4$ (where, x = 0.0, 0.2, 0.4 and 0.6) nanoparticles. It is observed that all the samples exhibit pure cubic structure with *Fd-3m* space group, without any impurity phase. The peaks (220), (311), (222), (400), (422), (511) and (440) show that all the samples exhibit inverse spinel phase. To confirm the structural and phase purity, Rietveld Refinement is performed and obtained patterns are presented in Fig. 3. Refinement patterns confirm that all the samples exhibit cubic structure and inverse spinel phase with *Fd-3m* space group, without the presence of any impurity phase. The obtained values χ^2 are well within the limit of 2, as depicted in Table 2. The Rietveld Refinement is also utilized for the estimation of cation distribution. The following is the cation distribution for all the samples.

Composition	Cation Distribution	
0.0	$[Co_{0.052}Fe_{0.948}]_A$	$[Co_{0.948}Fe_{1.052}]_B$
0.2	$[Co_{0.224}Cu_{0.028}Fe_{0.748}]_A$	$[Co_{0.576}Cu_{0.172}Fe_{1.252}]_B$
0.4	$[Co_{0.263}Cu_{0.168}Fe_{0.569}]_A$	$[Co_{0.337}Cu_{0.232}Fe_{1.431}]_B$
0.6	$[Co_{0.123}Cu_{0.252}Fe_{0.625}]_A$	$[Co_{0.277}Cu_{0.348}Fe_{1.375}]_B$

The obtained cation distribution shows the occupation of Cu^{2+}, Co^{2+} and Fe^{3+} ions over both A and B sites i.e., tetrahedral site and octahedral site, respectively, which confirm the formation of inverse spinel phase. But when the doping concentration increases, it becomes apparent that a greater number of Cu^{2+} and Co^{2+} ions begin to move towards the tetrahedral site (A-site), resulting in the formation of a mixed spinel phase. It is to be noted that there is no change in the structure and remains cubic for all the samples.

The crystallite size is calculated using the Scherrer's formula as represented in Eq. (1) [20],

$$d = \frac{n\lambda}{\beta Cos[03B8]} \tag{1}$$

where, n (0.89) is the shape factor, λ (1.54 Å) is the wavelength of X-rays that incident on the sample, β represents the Full width half maxima

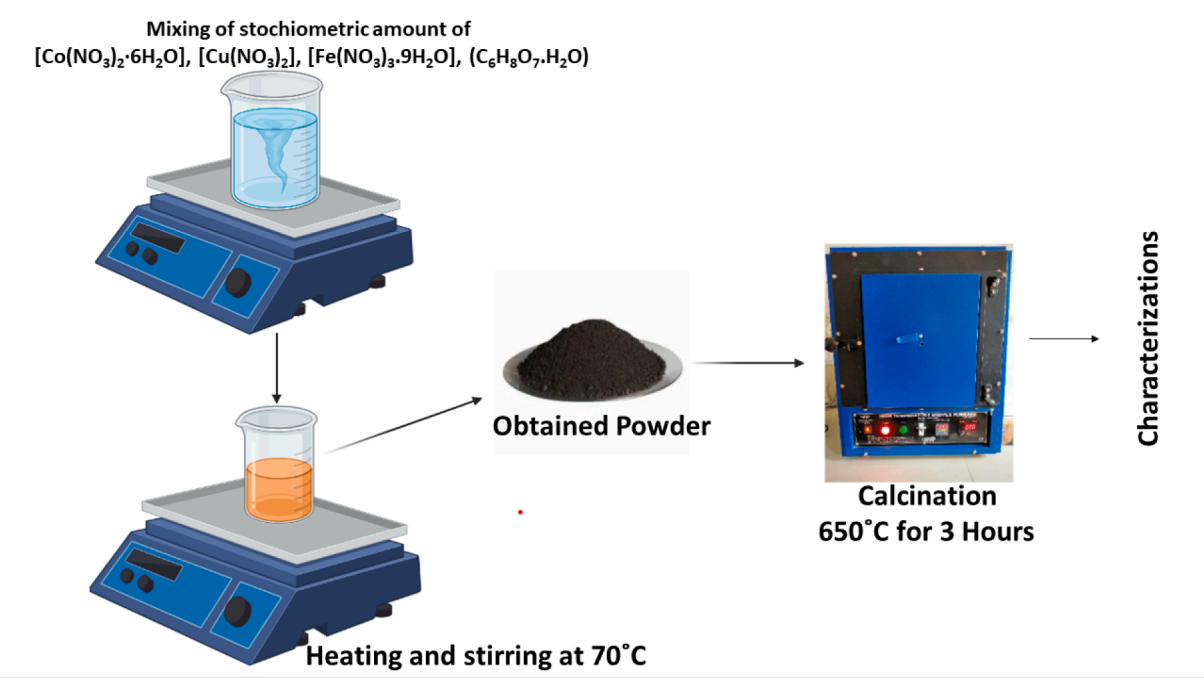

Fig. 1. The diagrammatic representation of the synthesis procedure.

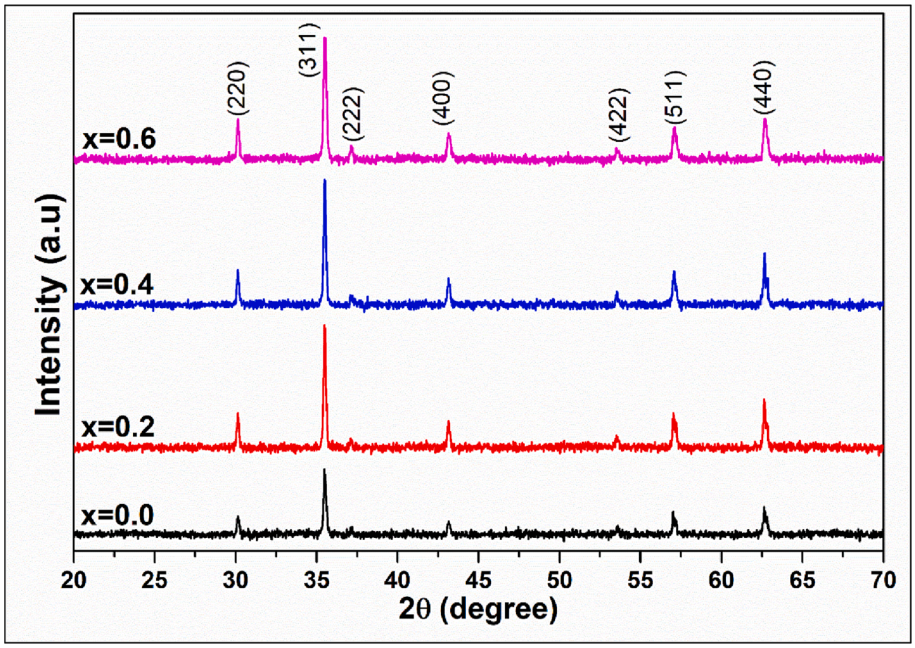

Fig. 2. The X-ray Diffraction pattern of the synthesized $Cu_xCo_{1-x}Fe_2O_4$ nanoparticles.

(FWHM) and θ depicts the diffraction angle.

The calculated crystallite sizes are presented in Table 1. It is noted that the crystallite size increases to 41.80 nm for × = 0.2, in contrast to the 39.55 nm of the pure sample. However, the crystallite size decreases as the dopant concentration rises. The first rise in crystallite size is a result of the replacement of Cu^{2+} ions in the tetrahedral position by Co^{2+} ions. However, the distribution of Cu^{2+} and Co^{2+} ions at both the tetrahedral and octahedral sites is what causes the subsequent reduction in crystallite size. The Cu^{2+} ions at both the sites produce the distortion due to the Jahn-Teller effect which as a result hinders the grain growth. In order to know the effect of strain and size on the peak broadening, Williamson-Hall (W-H) plots are obtained and presented in Fig. 4. It is assumed that both size and strain contribute towards the peak broadening and hence both have a Cauchy-like profile. The simple Eq. (2) that presents the outcome of the W-H plot is [21],

$$\beta_{hkl} Cos\theta = \frac{K\lambda}{d} + 4\varepsilon Sin\theta \quad (2)$$

where, former part of the right-hand side gives the crystallite size and the latter part gives the lattice strain.

The crystallite sizes obtained from the W-H method show the same variation as shown by the crystallite sizes obtained from Scherrer's method. However, a variation in crystallite sizes obtained from both the methods is because the Williamson-Hall plot takes micro-strain into

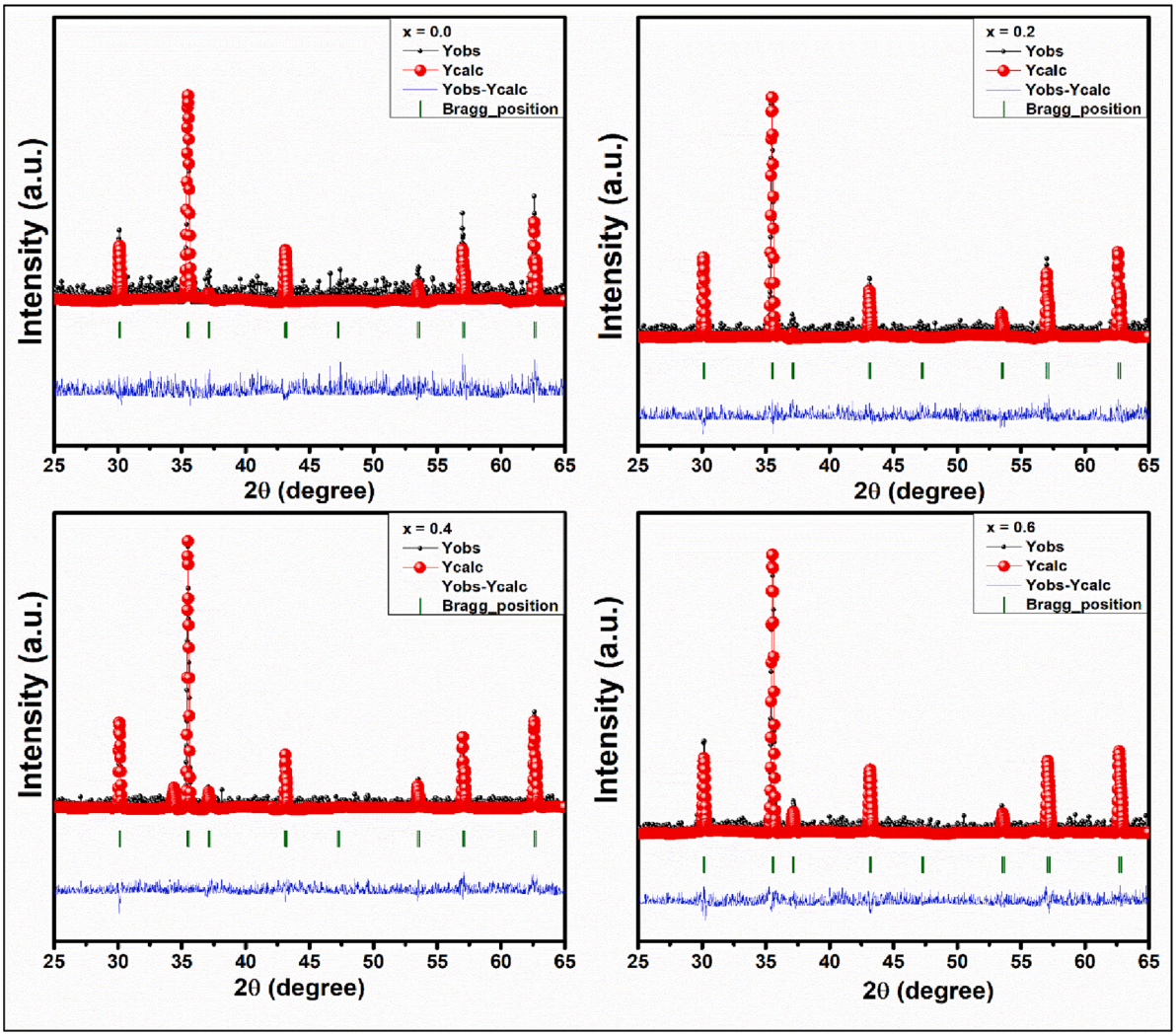

Fig. 3. The Rietveld Refinement patterns of the synthesized nanoparticles.

Table 1
The crystallite size, lattice parameters, strain and density parameters for $Cu_xCo_{1-x}Fe_2O_4$ nanoparticles.

Parameters	Symbol (Units)	Composition			
		x = 0.0	*x = 0.2*	*x = 0.4*	*x = 0.6*
Lattice Parameter	a(Å)	8.378	8.381	8.380	8.377
Lattice Volume	V(Å)^3	587.49	588.69	588.48	587.84
Crystallite Size	$d_{Scherrer}$(nm)	39.55	41.80	41.59	36.27
	d_{W-H}(nm)	51.33	55.88	55.66	45.89
Lattice Strain	∈	0.00537	0.0055	0.0061	0.0065
Dislocation density	$\delta_{Scherrer}$(nm^{-2})	0.00064	0.00057	0.00058	0.00076
	δ_{WH}(nm^{-2})	0.00038	0.00032	0.00032	0.00047
X-ray Density	ρ_x(g/cm^3)	5.403	5.377	5.361	5.343
Porosity	(%)	22.46	28.20	29.56	29.79

consideration. Moreover, it is observed that all the data points are varying linearly, which is attributed to the isotropic nature of all the samples. However, at higher concentrations of Cu^{2+} ions, the sample × = 0.6 is observed to show anisotropic nature, which is due to the distortion produced by Cu^{2+} ions. The W-H plot is also used to determine the lattice strain, and Table 1 displays the outcomes. The lattice strain is observed to increase from 0.00537 to 0.0065 when the dopant concentration rises. The increase in ion disordering caused by the Cu^{2+} ions is what causes the observed change.

The lattice parameters are estimated from the Nelson-Reley plot using the Eq. (3) and shown in Fig. 5 [22],

$$F(\theta) = \frac{1}{2}\left[\frac{Cos^2\theta}{Sin[03B8]} + \frac{Cos^2\theta}{\theta}\right] \quad (3)$$

The lattice parameters increase from 8.378 Å to 8.381 Å for × = 0.2 but drop to 8.377 Å when the concentration of Cu^{2+} ions increases to × = 0.6. The very first rise in the lattice parameter is due to Cu^{2+} ions displacing Co^{2+} ions from the octahedral position to the tetrahedral site and a few Fe^{3+} ions from the tetrahedral position to the octahedral position. However, when the substitution of Co^{2+} ions by Cu^{2+} ions

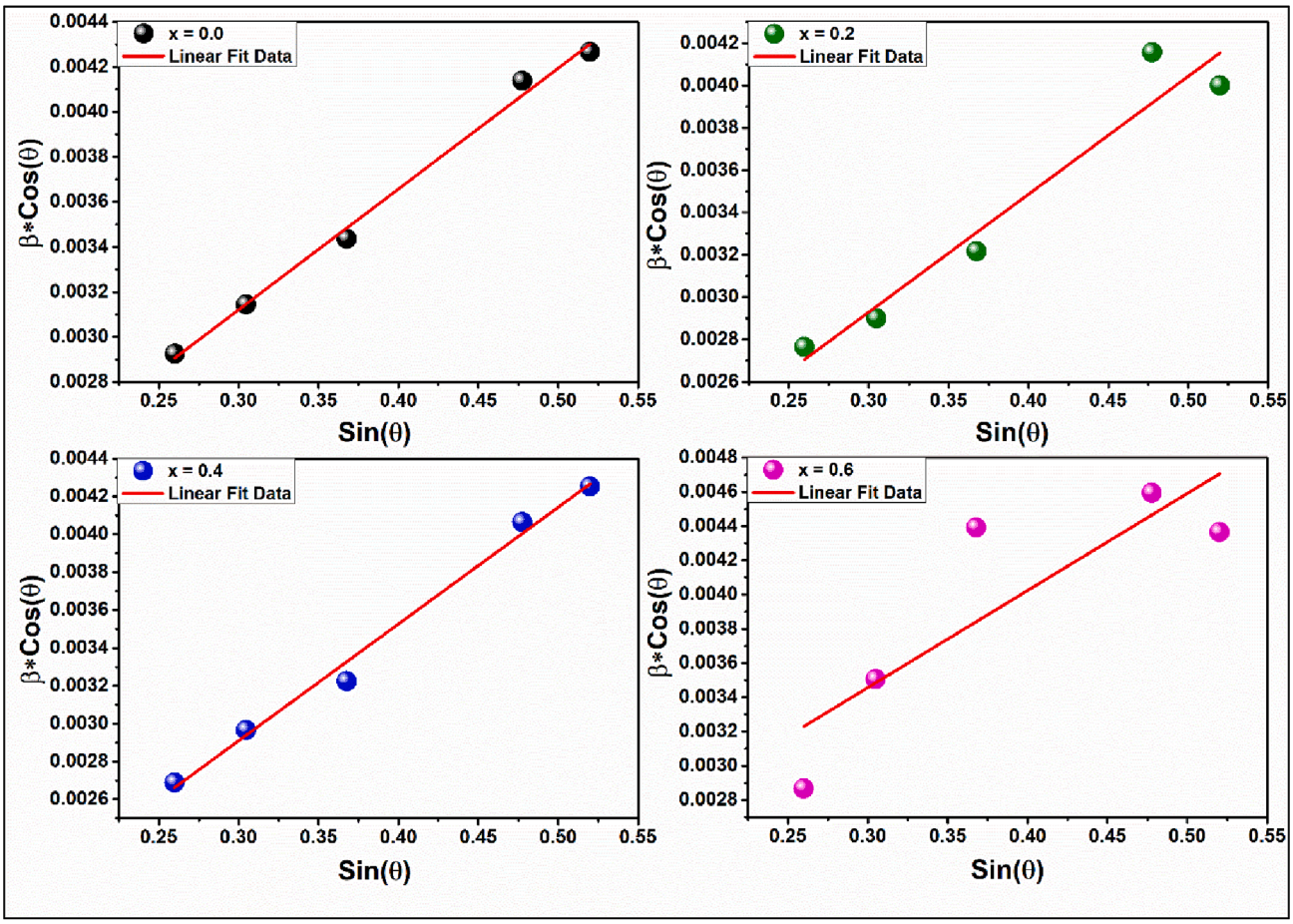

Fig. 4. The Williamson-Hall plots for $Cu_xCo_{1-x}Fe_2O_4$ nanoparticles.

increases, the lattice parameters fall from 8.381 Å to 8.377 Å. This variation is in agreement with Vegard's law which states that when the host ion of large ionic radii is replaced by the dopant ion of smaller ionic radii, the unit cell shows compression and vice-versa [23]. Since, the ionic radii of Co^{2+}, Cu^{2+} and Fe^{3+} ions at the octahedral site are, 0.745 Å, 0.73 Å and 0.645 Å, respectively, whereas, the ionic radii of Co^{2+}, Cu^{2+} and Fe^{3+} at the tetrahedral site are, 0.58 Å, 0.57 Å and 0.49 Å, respectively. Since the ionic radius of Cu^{2+} is lower than Co^{2+} ions, therefore the decrease in lattice parameter is highly expected. The volume of the unit cell is also calculated and it is noted that the observed volume is consistent with the lattice parameters.

The dislocation density of a material is used for assessing its crystallinity. Crystallinity increases when the dislocation density decreases, and vice versa. The dislocation density is calculated by the Eq. (4) and presented in Table 1 [21],

$$\delta = \frac{1}{D^2} \tag{4}$$

where, D is the crystallite sizes calculated from the Scherrer method and the W-H method.

It is observed that from the Scherrer method, dislocation first decreases from 0.00064 nm^{-2} to 0.00057 nm^{-2} and then increases to 0.00076 nm^{-2}. The decreasing trend shows an increase in the crystallinity of the sample. This trend is also visible in the dislocation density obtained from the crystallite size calculated form the W-H method. The X-ray density is estimated for all the samples using the Eq. (5) [24];

$$\rho_x = \frac{8M}{VN_A} \tag{5}$$

where, M is the molecular weight, V is the volume and N_A is the Avogadro's number (6.023×10^{23}).

It is observed that the density decreases from 5.403 g/cm^3 to 5.343 g/cm^3 with the increase in Cu^{2+} ions concentration. The variation in X-ray density of the pristine sample and the doped sample is very small as compared to the doping concentration which is because of the variation in volume. However, the atomic density of Cu and Co is approximately equal to 8.9 g/cm^3 due to which a large variation in x-ray density is not observed. The calculated X-ray density is presented in Table 1.

Using the following Eqs. (6) to (10), one may determine the tetrahedral bond length (d_{AX}), the octahedral bond length (d_{BX}), the tetrahedral edge length (d_{AXE}), the octahedral edge length (d_{BXE}), and the unshared edge length (d_{BXEU}) [25].

$$d_{AX} = 1.732a(u - 0.25) \tag{6}$$

$$d_{BX} = a\sqrt{(3u^2 - 2.75u + 0.6719)} \tag{7}$$

$$d_{AXE} = 1.4142a(2u - 0.5) \tag{8}$$

$$d_{BXE} = 1.4142a(1 - 2u) \tag{9}$$

$$d_{BXEU} = a\sqrt{(4u^2 - 3u + 0.6875)} \tag{10}$$

Table 2 displays the computed parameters. When the quantity of doping in a material is increased, the tetrahedral and octahedral bond lengths seem to decrease. This is how it is intended to be according to Vegard's law. In addition, when the concentration of Cu^{2+} ions increases, the values of octahedral edge length, tetrahedral edge length, and unshared edge length decrease. Furthermore, the change is relatively minor, owing to the occupancy of Co^{2+} ions and Cu^{2+} ions at the tetrahedral and octahedral sites, as shown by the cation distribution.

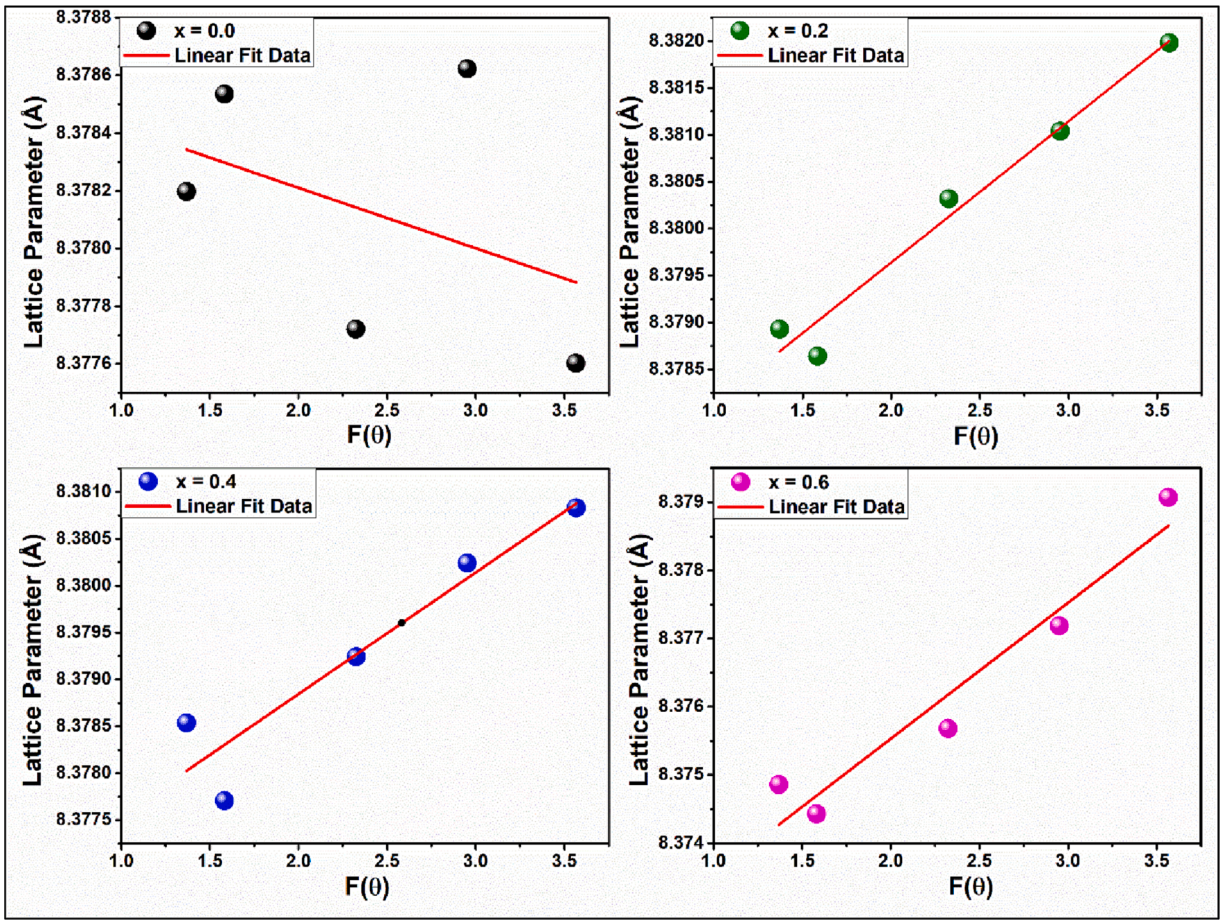

Fig. 5. The Nelson Relay plot $Cu_xCo_{1-x}Fe_2O_4$ nanoparticles for lattice parameters estimation.

Table 2
The tetrahedral bond length (d_{AX}), octahedral bond length (d_{BX}), tetrahedral edge length (d_{AXE}), octahedral edge length (d_{BXE}), unshared edge length (d_{BXEU}), Cation-Cation bond length, and Cation-Anion bond length for synthesized nanoparticles.

S. No		Parameters (Å)	$x = 0.0$	$x = 0.2$	$x = 0.4$	$x = 0.6$
1		d_{AX}	1.901	1.901	1.901	1.900
2		d_{BX}	2.046	2.047	2.046	2.045
3		d_{AXE}	3.104	3.106	3.105	3.103
4		d_{BXE}	2.820	2.830	2.820	2.810
5		d_{BXEU}	2.964	2.965	2.964	2.963
6		r_A	0.581	0.582	0.581	0.580
7		r_B	0.724	0.725	0.724	0.724
8	**Me-Me**	b	2.9623	2.9615	2.9614	2.9597
9		c	3.4735	3.4727	3.4726	3.4706
10		d	3.6281	3.6273	3.6271	3.6251
11		e	5.4421	5.4409	5.4406	5.4376
12		f	5.1308	5.1296	5.1294	5.1265
13	**Me-O**	p	2.0444	2.0443	2.0438	2.0426
14		q	1.9011	1.9007	1.9006	1.8995
15		r	3.6403	3.6394	3.6392	3.6372
16		s	3.6571	3.6563	3.6561	3.6541

Magnetic interactions in cubic spinel and spinel-like ferrites are proportional to the length and angle developed between the cation-cation and cation–anion. These parameters are determined by using the formulae (11)–(19) that are shown below [26].

Cation-Cation bond length

$$b = \frac{a\sqrt{2}}{4} \tag{11}$$

$$c = \frac{a\sqrt{11}}{8} \tag{12}$$

$$d = \frac{a\sqrt{3}}{4} \tag{13}$$

$$e = \frac{a3\sqrt{3}}{8} \tag{14}$$

$$f = \frac{a\sqrt{6}}{4} \tag{15}$$

Cation-Anion bond length

$$p = a\left(\frac{5}{8} - u\right) \tag{16}$$

$$q = a\sqrt{3}\left(u - \frac{1}{4}\right) \tag{17}$$

$$r = a\left(u - \frac{1}{4}\right)\sqrt{11} \tag{18}$$

$$s = a\sqrt{3}\left(\frac{u}{3} + \frac{1}{8}\right) \tag{19}$$

Table 2 illustrates the results of measurements used to determine the length of cation-cation and cation–anion bonds. The following formulae (20)–(24) may also be used to determine the bond angles between cations, denoted by Me-Me, and anions, denoted by Me-O [26];

$$\theta_1 = \cos^{-1}\left(\frac{p^2+q^2-c^2}{2pq}\right) \quad (20)$$

$$\theta_2 = \cos^{-1}\left(\frac{p^2+r^2-e^2}{2pr}\right) \quad (21)$$

$$\theta_3 = \cos^{-1}\left(\frac{p^2-c^2}{2p^2}\right) \quad (22)$$

$$\theta_4 = \cos^{-1}\left(\frac{p^2+s^2-f^2}{2ps}\right) \quad (23)$$

$$\theta_5 = \cos^{-1}\left(\frac{r^2+q^2-d^2}{2qr}\right) \quad (24)$$

The lengths and angles of the cation–anion (Me-O) and cation-cation (Me-Me) bonds, respectively, depict the A-A, A-B, and B-B interactions, as shown in Fig. 6. Table 3 shows the results of the calculated bond angles. Due to the radii of the ions, when divalent ions occupy the tetrahedral interstices, the expansion or compression in the tetrahedral site is significantly larger than that in the octahedral site. This is because the tetrahedral position contains fewer divalent ions than the octahedral site. The predicted bond lengths between cation and anion decrease when the concentration of Cu^{2+} ions increase, which is due to the lower ionic radii of Cu^{2+} ions as compared to the Co^{2+} ions and due to the presence of excess of Co^{2+} ions. The Me-Me and Me-O bond angles are observed to have a variable trend where the bond angle first decreases for $\times$ = 0.2, then increases for $\times$ = 0.4 and then again decreases for $\times$ = 0.6. This variation in bond angles is due to the cation distribution where Cu and Co ions are observed to distribute over both the tetrahedral site the and octahedral site. Further, the possibility of Cu^{2+} ions occupying the Fe-site cannot be neglected as well.

The Scanning Electron Microscope (SEM) is used to determine the morphology of all materials, and the micrographs are shown in Fig. 7. The micrographs demonstrate the production of non-homogeneous grains, with grain size decreasing as doping ion concentration increases. The reduction in grain size indicates that Cu^{2+} ions have replaced Co^{2+} ions in cobalt ferrites [18]. Furthermore, the SEM pictures show the creation of porous grains, making the synthesized ferrite nanoparticles a promising choice for wastewater treatment and gas sensing that needs a wide surface area for the adsorption process. The

Table 3
The computed bond angles between A-A, A-B and B-B for the $Cu_xCo_{1-x}Fe_2O_4$ nanoparticles.

S. No	Parameters (Degrees)	*Composition (x)*			
		x = 0.0	*x = 0.2*	*x = 0.4*	*x = 0.6*
1	θ_1	123.332°	123.312°	123.333°	123.325°
2	θ_2	144.945°	144.924°	144.974°	144.954°
3	θ_3	123.346°	123.319°	123.346°	123.579°
4	θ_4	125.916°	125.894°	125.916°	125.908°
5	θ_5	74.473°	74.562°	74.491°	74.258°

porosity of all the synthesized samples are estimated using ImageJ software and the values are presented in Table 1. It is observed that the porosity percentage increases from 22.46% to 29.79% with the increase in Cu^{2+} ions concentration. The increase in porosity also shows a decrease in grain size with the increase in doping concentration. However, a sharp increase in the porosity is observed with the initial doping of Cu^{2+} ions i.e., from 22.46% to 28.20%, and afterwards, the increase in porosity is observed to vary slowly.

4.2. Fourier Transform Infrared Spectroscopy (FTIR)

Fig. 8 depicts an FTIR spectrum of each sample. The band of absorption that occurs around 600 cm^{-1} is due to the vibration of the metal–oxygen (Me-O) bond in the tetrahedral site, while the band that occurs around 400 cm^{-1} is due to the vibration of the iron-oxygen (Fe-O) bond [27,28]. It is observed that the band ν_1 ranges between 532 cm^{-1} and 541 cm^{-1} which can be associated with the intrinsic vibrations of the tetrahedral complexes. Whereas, the band ν_2 ranges between 402 cm^{-1} and 408 cm^{-1} is attributed to the intrinsic vibrations of the octahedral complexes. The observed band positions confirm the formation of cubic symmetry.

In addition, it has been observed that ferrites have considerable elastic characteristics, which may be attributed to the interatomic and interionic forces that they contain. However, the elastic characteristics of ferrites may be approximated by applying stress to the material. On the other hand, FTIR spectra in conjunction with structural characteristics may also be used to investigate the elastic properties of ferrites [29,30]. In most cases, the strength and stability of interatomic and interionic bonds may be inferred from elastic characteristics. Therefore,

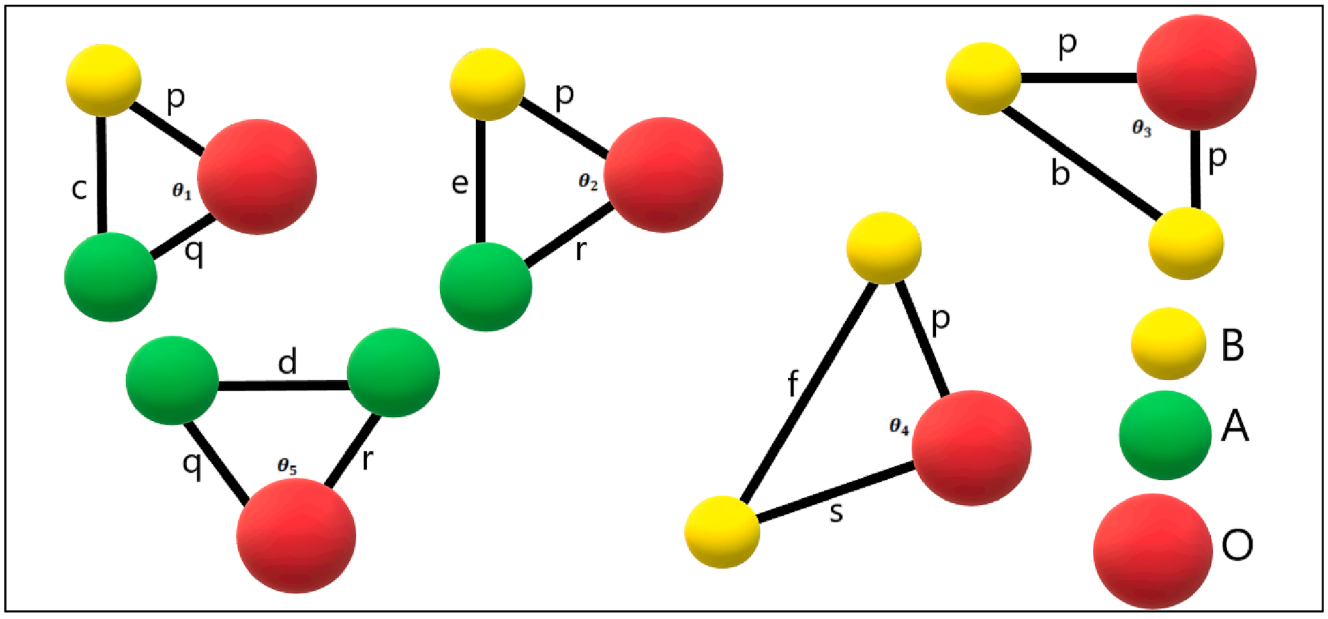

Fig. 6. The computed bond angles representing the type of interaction for the synthesized nanoparticles.

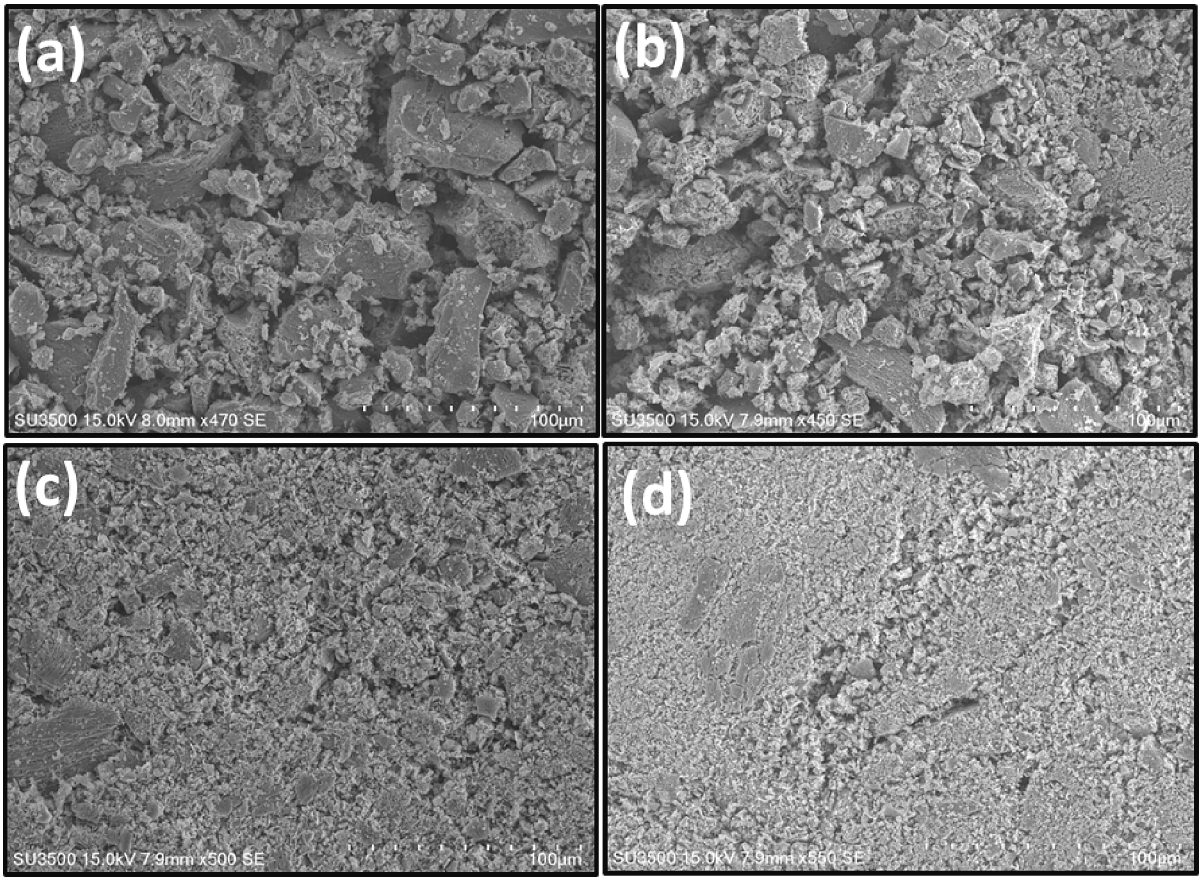

Fig. 7. The SEM micrographs of $Cu_xCo_{1-x}Fe_2O_4$ nanoparticles.

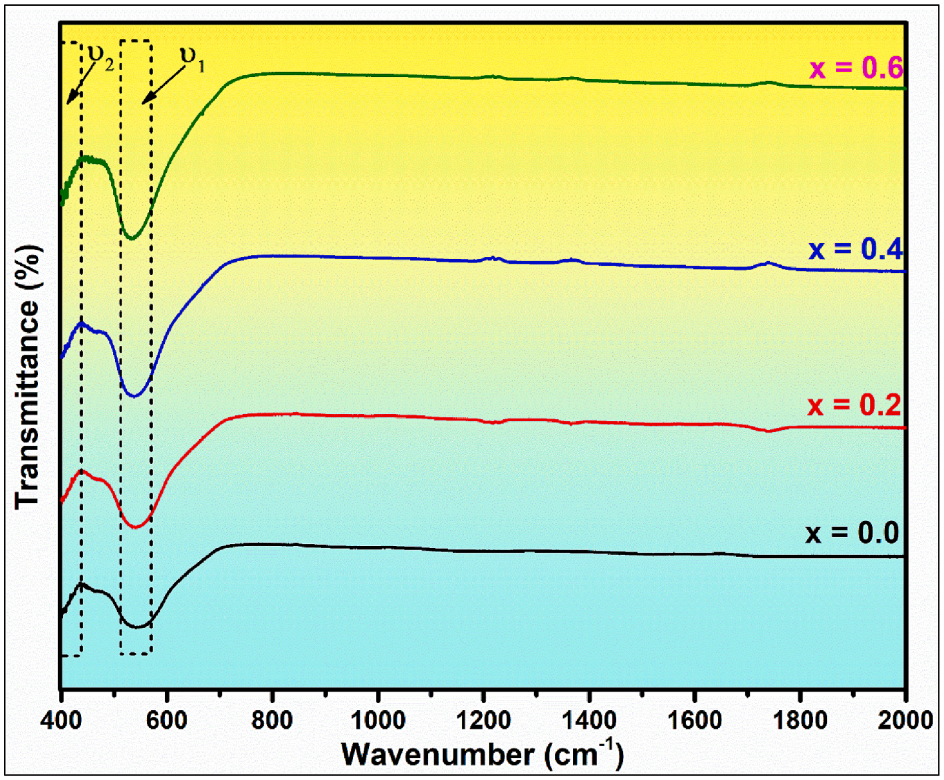

Fig. 8. The FTIR spectra of the synthesized $Cu_xCo_{1-x}Fe_2O_4$ nanoparticles.

it is worth to make an approximation of the crystal's elastic characteristics. In this regard, the force constant of tetrahedral (k_t), octahedral (k_o) sites and average force constant ($k^{'}$) are calculated using the Waldron relations (25)–(27) [31];

$$k_t = 7.62 \times M_A \times v_1^2 \times 10^{-7} \tag{25}$$

$$k_o = 5.31 \times M_B \times v_2^2 \times 10^{-7} \tag{26}$$

$$k^{'} = \frac{1}{2}(k_t + k_o) \tag{27}$$

where, M_A and M_B is the molecular weight of A-site and B-site, respectively.

The calculated values are tabulated in Table 4. It is observed that the average value of force constant decreases with the increase in Cu^{2+} ions doping on $CoFe_2O_4$. The decreasing trend can be related to the bond length, bond angle and cationic distribution. As observed from XRD analysis, bond length decreases which must increase the force constant but simultaneously the bond angles show variable trends and further the cation distribution shows the occupancy of Cu^{2+} ions and Co^{2+} ions at both octahedral and tetrahedral sites. These all parameters contribute to the decreasing trend of the force constant.

The capacity of a material to withstand any sort of deformation may be quantified by measuring its rigidity, which can also be referred to as its stiffness constant. On the basis of the stress–strain concept, Hook's law states that there is a relationship between the stress n_j, the strain (ε_{ij}), and the stiffness (C_{ij}) [32]. Only the three stiffness constants C_{11}, C_{12}, and C_{44} are considered to be dominant for cubic symmetry. C_{11} represents the degree of elasticity in length, while C_{12} represents the elasticity in shape. C_{44} is the dominating stiffness constant. But for spinel ferrites with cubic symmetry, $C_{11} \approx C_{12}$. The stiffness constant C_{11} is calculated by using the following relation [31];

$$C_{11} = \frac{k^{'}}{a} \tag{28}$$

where, $k^{'}$ is the average force constant and a is the lattice parameter.

It is observed that the stiffness constant value decreases with the increase in Cu^{2+} ions concentration. The value of stiffness constant is used to calculate the longitudinal (V_l) and shear (V_s) velocity using the relations [32];

$$V_l = \sqrt{\frac{C_{11}}{\rho_x}} \tag{29a}$$

$$V_s = \frac{V_l}{\sqrt{3}} \tag{29b}$$

The bulk modulus (B) is again related to the stiffness constant by the relation [33];

$$B = \frac{1}{3}(C_{11} + 2C_{12}) \tag{30}$$

However, C_{11}=C_{12}, therefore, $B = C_{11}$. The values of rigidity modulus (G), Poisson's ratio (σ) and Young's modulus (E) are calculated using the following relation [32];

$$G = \rho_x (V_s)^2 \tag{31}$$

$$\sigma = \frac{(3B - 2G)}{(6B + 2G)} \tag{32}$$

$$E = (1 + \sigma)2G \tag{33}$$

As the amount of Cu^{2+} ions doping increases, it can be seen that the estimated values of both the bulk modulus and the rigidity modulus decrease. Table 5 displays the estimated values for the various elastic parameters. In addition, it is observed that the value of Young's modulus decreases as the amount of doping in the system rises, and this drop may be connected to a reduction in the total force constant of the system [33]. In addition, the drop in elastic modulus that was discovered provided further evidence that the interatomic bonds that connect multiple atoms weaken continually along with the rise in the concentration of Cu^{2+} ions in cobalt ferrite nanoparticles. Therefore, the alteration that is observed also validates the cationic distribution, which indicates that both Cu^{2+} ions and Co^{2+} ions have dispersed throughout the octahedral and tetrahedral sites, however only a small number of the divalent ions have replaced the Fe^{3+} ions at both the sites. This is because a limited number of divalent ions have replaced the Fe^{3+} ions at both sites.

The ductility and brittleness behavior of the synthesized samples is observed through Pugh's ratio (B/G) and Poisson's ratio (σ), as presented in Table 5 [34,35]. It is observed that the value of B/G and σ are lower than their critical value of 1.75 and 0.26, respectively [36]. However, both the values are constant i.e., 1.66 and 0.249, respectively. This shows that Cu^{2+} ions doping has not affected the ductility and brittleness of the cobalt ferrite. In addition, the value of σ for all the samples is 0.249 which is in the range of 0.20–0.30. The value lies within the limit of −1.0 to 0.5, which implies that all the samples are isotropic elastic in nature. The value of σ is consistent with the theory of isotropic elasticity [37].

4.3. Magnetic characteristics

As apparent from Fig. 9, the VSM analysis is performed at room temperature in order to provide an accurate reading of the magnetic properties of the whole sample. The existence of a hysteresis loop that has not been interrupted demonstrates the generation of magnetic samples that are free of any impurity phase that would have an impact on the magnetic properties of all of the samples. All of the samples' values for the parameters such as specific magnetization (σ_S), coercivity (H_C), specific remanence (σ_R), and squareness ratio (SQR) were measured with the use of the hysteresis loop. These values can be found in Table 6.

The value of coercivity (H_C) is observed to decrease first from 1154.46 Oe to 971.59 Oe for x = 0.2 and then increases to 1705.02 Oe. The change in the value of H_C can be related to the crystallite size by the relation [38];

$$H_C = a + \frac{b}{D} \tag{34}$$

where a and b are arbitrary constants and D signifies the crystallite size or the particle size.

It is observed that when × approaches the value of 0.2, the size of the

Table 4
The peak position, force constant and velocity calculated from FTIR for synthesized nanoparticles.

Composition (x)	Peak Position (cm^{-1})		Force constant (N/m)			Velocity (m/s)		
	v_1	v_2	k_t	k_o	$k^{'}$	V_l	V_s	V_m
0.0	541.5	408.5	125.66	105.35	115.51	5052.38	2917.07	3238.41
0.2	540.5	403.0	128.35	100.55	114.45	5039.54	2909.66	3230.63
0.4	538.5	401.0	127.72	98.19	112.95	5014.06	2894.95	3213.98
0.6	532.5	402.5	124.46	98.84	111.65	4995.41	2884.18	3201.77

Table 5
The values of elastic characteristics of $Cu_xCo_{1-x}Fe_2O_4$ nanoparticles calculated from FTIR.

Composition	Stiffness Constant (GPa)	Longitudinal Modulus (GPa)	Rigidity Modulus (GPa)	Bulk Modulus (GPa)	Young's Modulus (GPa)	Poisson's Ratio	Pugh's Ratio
	C_{11}	L	G	B	E	σ	(B/G)
0.0	137.92	137.89	45.97	76.59	114.83	0.249	1.66
0.2	136.56	136.55	45.53	75.84	113.73	0.249	1.66
0.4	134.78	134.77	44.93	74.86	112.24	0.249	1.66
0.6	133.33	133.31	44.44	74.05	111.01	0.249	1.66

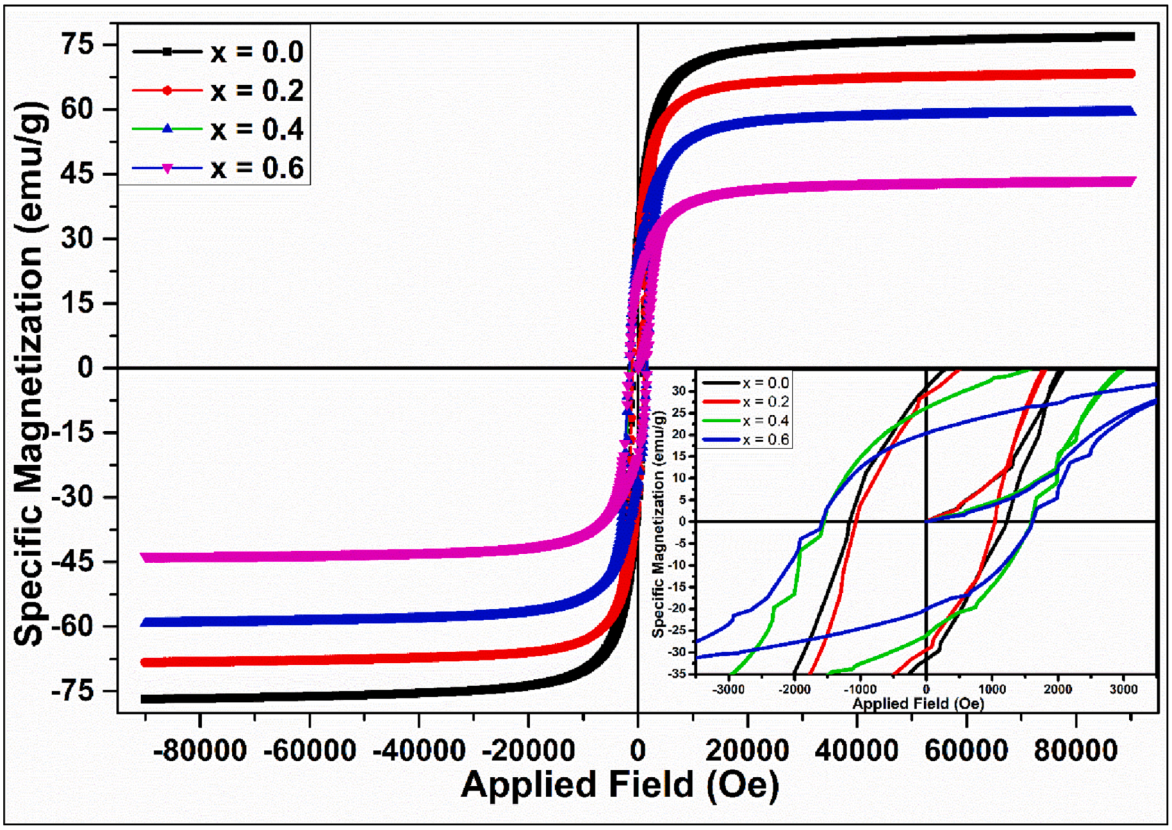

Fig. 9. The VSM plot shows the Hysteresis loops for all the synthesized nanoparticles.

Table 6
The obtained valued of specific magnetization (σ_S), Coercivity (H_C), specific remanence (σ_R) and Squareness ratio (SQR) for $Cu_xCo_{1-x}Fe_2O_4$ nanoparticles.

Composition (x)	Saturation Magnetization (emu/g)	Coercive Field (Oe)	Remnant Magnetization (emu/g)	SQR	$n_B(\mu_B)$
0.0	76.85	1154.46	31.05	0.404	3.29
0.2	68.31	971.59	29.34	0.429	2.92
0.4	59.31	1634.98	26.15	0.441	2.52
0.6	43.62	1705.02	20.39	0.467	1.85

crystallite increases, but this pattern reverses itself as the concentration of Cu^{2+} ions continues to rise. Crystallites that are larger have a higher tendency to include more magnetic domains. When compared to the motion of the domain itself, the magnetization that is induced by the motion of the domain wall requires less energy. The wider domain walls that are present in bigger crystallites make it simple to magnetize or demagnetize the material. As a result, the samples that have bigger crystallite sizes exhibit a lower value of coercivity. Also, regional magnetic anisotropy is weak for bigger crystallites; thus, the magnetic exchange becomes essential, which leads to a low value of coercivity [39]. In addition, the value of σ_S is determined using the hysteresis loop. It has been discovered that the σ_S value drops from 76.85 emu/g to 43.62 emu/g as the concentration of Cu^{2+} ions in $CoFe_2O_4$ nanoparticles rises. Previously, this value was 76.85 emu/g. The two sublattice model proposed by Neel may provide an explanation for the drop-in magnetization. According to this paradigm, the A-B interaction is the most powerful of the three types of interactions (A-A, B-B, and A-B). The net magnetization is the contribution of vector sum of A and B interactions, i.e., $M = M_A + M_B$. The magnetic moment of Cu^{2+} ion is 1.73 μ_B, Co^{2+} is 3.87 μ_B and Fe^{3+} is 5 μ_B [40]. The substitution of Cu^{2+} ions in place of Co^{2+} ions lead to the weakening of A-B exchange interaction which results in the decrease in net magnetic moment and hence the decrease in net magnetization. This also justifies the cation distribution obtained from XRD where, Cu^{2+} ions are observed to occupy the tetrahedral and octahedral sites where they replace the Co^{2+} ions. Moreover, the migration of Fe^{3+} from the octahedral to the tetrahedral site and vice-

versa due to the irregular distribution of Cu^{2+} ions and Co^{2+} ions at both the sites. The similar trends have been observed for Cu, Ce and Zn-doped cobalt ferrite nanoparticles [41–43]. For the present samples, the variation of σ and H_c with the change in doping concentration is shown in Fig. 10. The also supports the decrease in net magnetic moment values calculated using the formula [44];

$$n_B = \frac{\sigma_s \times M_w}{5585} \tag{35}$$

where, σ_s and M_W are the values of saturation magnetization and molecular weight of the sample, respectively.

The calculated values are observed to decrease from 3.29 μ_B to 1.85 μ_B. In addition, a graph is plotted between σ_s and $\frac{1}{H_c}$, as shown in Fig. 11. The slope of this graph provides a constant value '*b*' which is used to calculate the value of effective anisotropic constant '$K_{effective}$' using the following relation [45];

$$K_{effective} = \sigma_S \left(\frac{15b}{4}\right)^{0.5} \tag{36}$$

The value of b and the effective anisotropy constant are calculated and presented in Table 7. It is observed that as the concentration of dopant ions increase, the value $K_{effective}$ decreases from 10.672×10^6 erg/g to 4.461×10^6 erg/g. The decreasing tendency is because the Cu^{2+} and Co^{2+} ions have distributed over both the A and B-site which contributes to vacancy generation and other imperfections that exert fields on these ions. Further, using the value of $K_{effective}$, the value of the intrinsic magnetic field is also calculated from the relation [46],

$$H_a = \frac{2K_{effective}}{M_S} \tag{37}$$

The obtained value of H_a is observed to decrease from 277.74 Oe to 204.53 Oe. The decreasing value fo H_a with the increase in Cu^{2+} ions concentration suggests the soft magnetic character of the synthesized samples is increasing with the doping. The value of magnetizing field (*N*) is also calculated, for a single non-interacting domain, using the relation [45],

$$H_c = \left[\left(\frac{K_{effective}}{\mu_o M_S}\right) - N\sigma_S\right] \tag{38}$$

The demagnetizing field N value is observed to show a similar trend as that of the value of coercivity. It should be noted that with the higher value of coercivity, a strong demagnetizing field is required to surpass the magneto-crystalline anisotropy barrier and vice-versa. Thus, the values of N are in good agreement with the values of coercivity.

The squareness (SQR) values are also calculated for all the samples and it is observed that the value of SQR lies in the range of 0.404–0.467. For all the samples, the values of SQR are well below 0.5, which indicates that the ferrite nanoparticles exhibit single-domain uniaxial anisotropy according to Stonner-Wohlfarth (S-W) model [47].

5. Conclusion

Herein, we synthesized the Cu-doped $CoFe_2O_4$ nanoparticles ($Co_{1-x}Cu_xFe_2O_4$, where $\times$ = 0.0, 0.2, 0.4 and 0.6) by employing the citrate precursor method. The X-ray Diffraction (XRD) confirmed the formation of pure cubic crystals without any impurity phase with *Fd-3m* space group. Rietveld refinement showed structural purity and cation distribution in all the samples. The crystallite sizes were obtained from the Scherrer method and Williamson-Hall method and it was observed that the size first increased from 39.55 nm to 41.80 nm and then decreased to 36.27 nm with an increase of Cu^{2+} ions. Similar variations were observed in the lattice parameter where the value of 'a' first increased from 8.378 Å to 8.381 Å and with further substitution, the value decreased to 8.377 Å. Scanning Electron Microscopy (SEM) showed the formation of non-uniform grain where the grain size decreased with the increase in doping. Fourier Transform Infrared Spectroscopy (FTIR) showed the presence of two peaks ν_1 and ν_2 around 541 cm^{-1} and 408 cm^{-1}, respectively, which further decreased to 532.5 cm^{-1} and 402.5 cm^{-1} as the dopant ion concentration increased. Poisson's ratio and Pugh's ratio showed a constant value around 0.249 and 1.66, respectively, which revealed the elastic nature of all the samples. Vibrating Sample Magnetometer (VSM) analysis showed a decrease in σ_S value from 76.85 emu/g to 43.62 emu/g and a decrease in the net magnetic

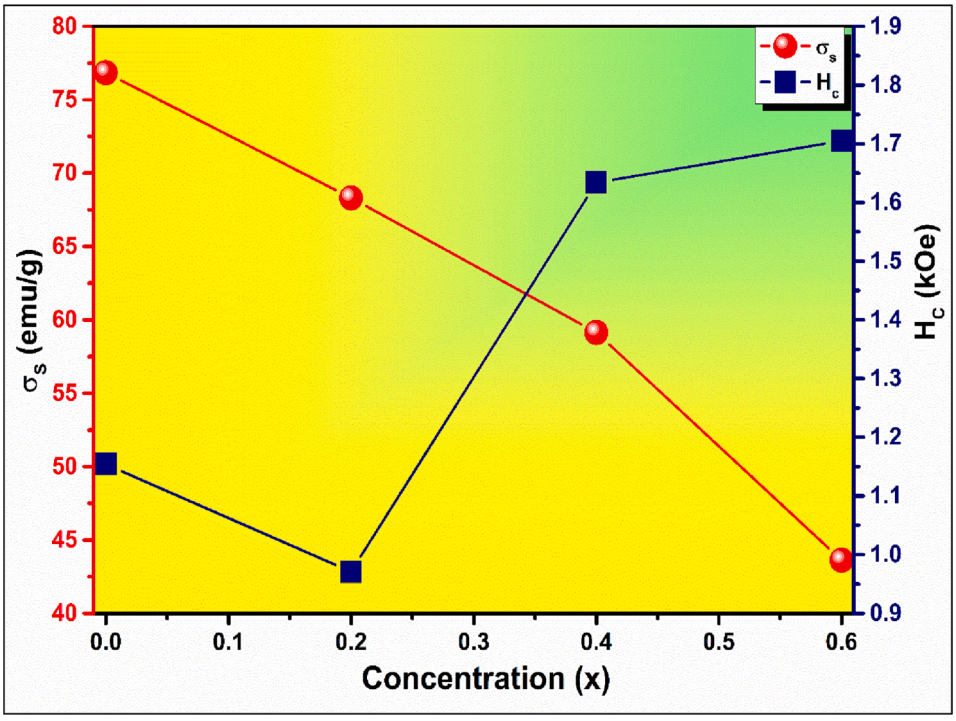

Fig. 10. The variation of σ_s and H_c with respect to concentration for all the nano particles.

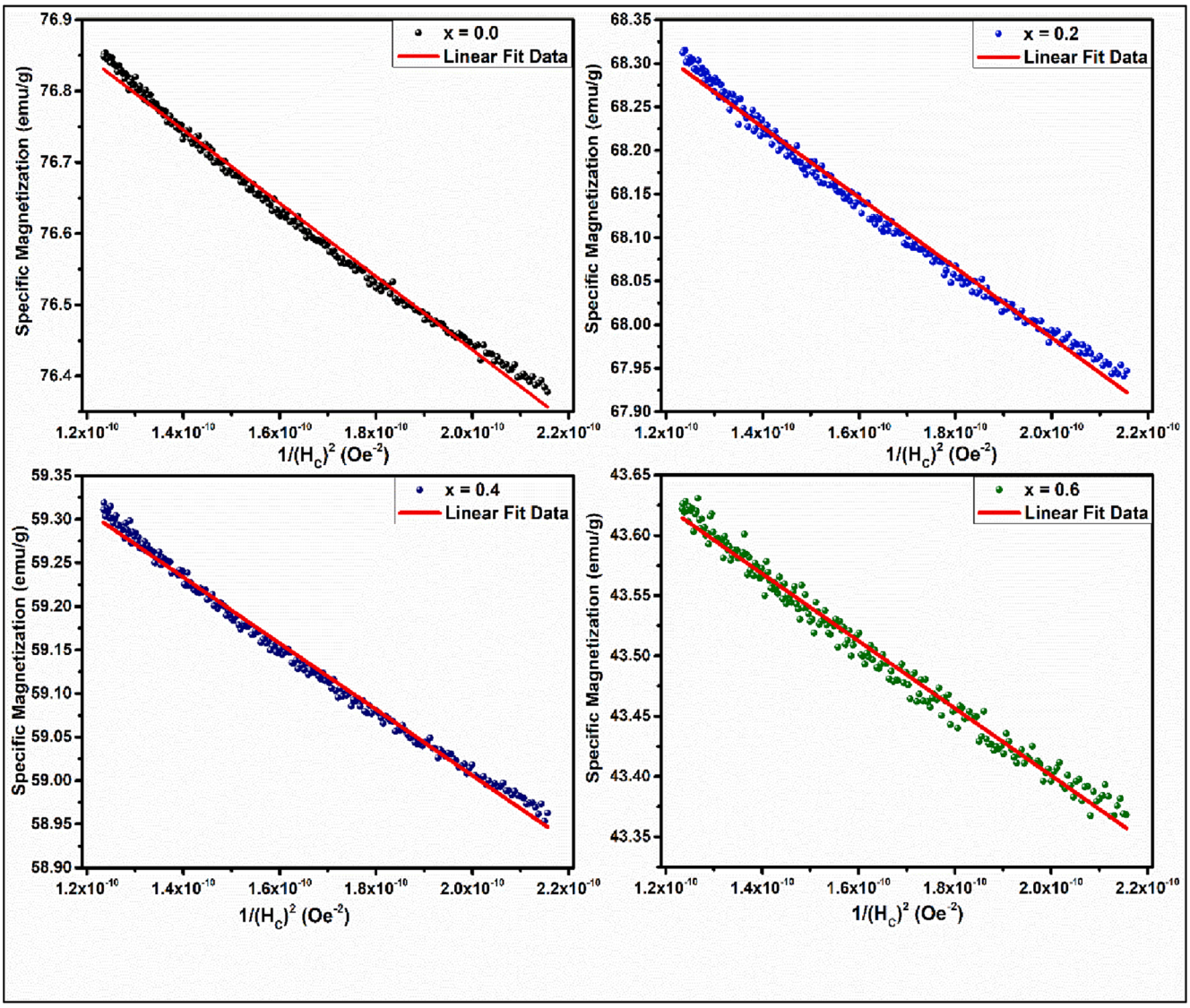

Fig. 11. The variation of $1/Hc^2$ against specific magnetization for $Cu_xCo_{1-x}Fe_2O_4$ nanoparticles.

Table 7
The values of effective anisotropic constant '$K_{effective}$', intrinsic magnetic field (H_a), magnetizing field (N) for the synthesized $Cu_xCo_{1-x}Fe_2O_4$ nanoparticles.

Composition (x)	K_{eff}($\times 10^6$) erg/g	H_a(Oe)	$b\times 10^9$	N(Oe^2.g/erg)
0.0	10.672	277.74	5.14	3585.71
0.2	8.393	245.73	4.03	3567.43
0.4	7.073	238.51	3.79	3963.85
0.6	4.461	204.53	2.78	4607.25

moment (n_B) from 3.29 μ_B to 1.85 μ_B. The effective anisotropy constant value decreased from 10.62erg/g to 4.461erg/g which is attributed to the soft character of prepared ferrites. Thus, the prepared nanoparticles showed that their structural, elastic, and magnetic properties could be significantly modulated with the proper doping concentration of copper ions. Since, the porosity of the prepared nanoparticles increased with the increase in doping concentration it could be beneficial for the adsorption process. The increase in the adsorption process could lead to improvement in sensing applications and water purification applications.

CRediT authorship contribution statement

Atul Thakur: Conceptualization, Methodology, Supervision. **Ritesh Verma:** Conceptualization, Methodology. **Fayu Wan:** Visualization, Investigation. **Blaise Ravelo:** Visualization, Investigation. **Irina Edelman:** Writing – review & editing. **Sergey Ovchinnikov:** Writing – review & editing. **Preeti Thakur:** Writing – original draft.

Declaration of Competing Interest

The authors declare that they have no known competing financial interests or personal relationships that could have appeared to influence the work reported in this paper.

Data availability

No data was used for the research described in the article.

Acknowledgments

This research work was supported by the National Key Research and Development Program of China (2022YFE010707). The author(s) would

like to acknowledge the support provided under the DST-FIST Grant No. SR/FST/PS-I/2018/48 of Govt. of India. PT is thankful to DST-SERB TARE fellowship vide Sanction Order No TAR/2022/000414.

References

[1] S. Amiri, H. Shokrollahi, The role of cobalt ferrite magnetic nanoparticles in medical science, Mater. Sci. Eng. C 33 (2013) 1–8.

[2] W.H. Huang, J.L. Jiang, T. Mandal, Ferrite nanoparticles: catalysis in multi component reaction (MCR), Synth. Commun. 51 (2021) 2397–2422.

[3] P. Sharma, A. Sharma, M. Sharma, N. Bhalla, P. Estrela, A. Jain, P. Thakur, A. Thakur, Nanomaterial fungicides: In vitro and in vivo antimycotic activity of cobalt and nickel nanoferrites on phytopathogenic fungi, Glob. Challeng. 1 (2017) 1700041.

[4] P. Sharma, P. Thakur, J.L. Mattei, P. Queffelec, A. Thakur, Synthesis, structural, optical, electrical and Mossbauer spectroscopic studies of Co-substituted Li0.5Fe2.5O4, J. Magn. Magn. Matr. 407 (2016) 17–23.

[5] X.Y. Zhou, J. Wang, L.L. Zhou, Y.G. Wang, D.S. Yao, Structure, magnetic and microwave absorption properties of NiZnMn ferrite ceramics, J. Magn. Magn. Matr. 534 (2021), 168043.

[6] K.N. Trohidou, Mahnetic nanoparticles Assemblies, Ist edition, Pan Stanford, 2014.

[7] A. Thakur, P. Thakur, J.H. Hsu, Magnetic behaviour of Ni0.4Zn0.5Co0.1Fe1.9O4 spinel nano ferrite, J. Appl. Phys. 111 (2012) 07A305.

[8] I.H. Gul, A. Maqsood, M. Naeem, M.N. Ashiq, Optical, magnetic, and electrical investigation of cobalt ferrite nanoparticles synthesized by co-precipitation route, J. Alloy. Compd. 507 (2010) 201–206.

[9] M. Hashim, S. Alimuddin, B.H. Kumar, S.E. Koo, E.M. Shirsath, J. Mohammed, R. K. Shah, H.K. Kotnala, H. Choi, R.K. Chung, Structural, electrical and magnetic properties of Co–Cu ferrite nanoparticles, J. Alloy Compd. 518 (2012) 11–18.

[10] N. Sanpo, J. Wang, C.C. Berndt, Sol-Gel Synthesized Copper-Substituted Cobalt Ferrite Nanoparticles for Biomedical Applications, J. Nano Res. 22 (2013) 95–106.

[11] P. Thakur, N. Gahlawat, P. Punia, S. Kharbanda, B. Ravelo, A. Thakur, Cobalt nanoferrites: a review on synthesis, characterization, and Applications, J. Supercond. Nov. Magn. 35 (10) (2022) 2639–2669.

[12] J. Balavijayalakshmi, N. Suriyanarayana, R. Jayaprakash, Influence of copper on the magnetic properties of cobalt ferrite nano particles, Mater. Res. 81 (2012) 52–54.

[13] B.K. Bammannavar, L.R. Naik, R.B. Pujar, Influence of time and temperature on resistivity and microstructure of $Cu_xCo_{1-x}Fe_2O_4$ mixed ferrites, Prog. Electromagnet. Res. Lett. 4 (2008) 121–129.

[14] R. Verma, P. Thakur, A. Chauhan, R. Jasorita, A. Thakur, A review on MXene and its composite for electromagnetic interference (EMI) shielding applications, Carbon 208 (2023) 1170–1190.

[15] W.S. Mohamed, N.M.A. Hadia, B. Al-Bakheet, M. Alzaid, A.M. Abu-Dief, Impact of Cu2+ cation substitution on structural, morphological, optical and magnetic properties of $Co_{1-x}Cu_xFe_2O_4$ nanoparticles synthesized by a facile hydrothermal approach, Solid State Sci. 125 (2022), 106841.

[16] C. Aziz, B. Azhdar, Synthesis of dysprosium doped cobalt ferrite nanoparticles by sol-gel auto-combustion method and influence of grinding technique on structural, morphological and magnetic properties, J. Magn. Magn. Matr. 542 (2022), 168577.

[17] K.V. Siva, A. Kumar, J.A. Chelvane, A. Arockiarajan, Structural, magnetic, magnetostrictive and optical properties of Mn and Cu co-doped cobalt ferrite, Mater. Sci. Eng. B 284 (2022), 115885.

[18] Z. Jing, M. Guo, Z. Li, C. Qin, Z. Chen, Z. Li, H. Gong, Study on structure and magnetic properties of rare earth doped cobalt ferrite: The influence of different substitution positions, Ceram. Int. 49 (2023) 14046–14056.

[19] A. Thakur, P. Thakur, S.M.P. Khurana, Synthesis and applications of nanoparticles, Springer Nat. 1 (2022) 1–545.

[20] R. Verma, A. Chauhan, K.M. Batoo, M. Hadi, E.H. Raslan, R. Kumar, M.F. Ijaz, A. K. Assaifan, Structural, optical and electrical properties of vanadium doped lead free BCZT ceramics, J. Alloy Compd. 869 (2021), 159520.

[21] R. Verma, A. Chauhan, K.M. Batoo, R. Kumar, M. Hadi, E.H. Raslan, Structural, morphological, and optical properties of strontium doped lead-free BCZT ceramics, Ceram. Int. 47 (2021) 15442–15457.

[22] M. Hadi, K.M. Batoo, A. Chauhan, O.M. Aldossary, R. Verma, Y. Yang, Tuning of Structural, Dielectric, and electronic properties of Cu-doped Co-Zn ferrite nanoparticles for multilayer inductor chip application, Magnetochem. 7 (2021) 53.

[23] R.D. Shannon, Revised effective ionic radii and systematic studies of interatomic distances in halides and chalcogenides, Acta Crysta., A 32 (5) (1976) 751–767.

[24] M.K. Bharti, S. Chalia, P. Thakur, A. Thakur, Effect of Lanthanum doping on microstructural, dielectric and magnetic properties of $Mn_{0.4}Zn_{0.6}Cd_{0.2}La_xFe_{1.8-x}O_4$ ($0.0 \leq x \leq 0.4$), J. Supercond. Nov. Magn. 34 (2021) 2591–2600.

[25] R. Verma, P. Thakur, A.C.A. Sun, A. Thakur, Investigation of structural, microstructural and electrical characteristics of hydrothermally synthesized $Li_{0.5-0.5\ x}Co_xFe_{2.5-0.5x}O_4$, ($0.0 \leq x \leq 0.4$) ferrite nanoparticles, Phys. B, Cond. Matr. 661 (2023), 414926.

[26] A. Rais, K. Taibi, A. Addou, A. Zanoun, Y. Al-Douri, Copper substitution effect on the structural properties of nickel ferrites, Ceram. Int. 40 (9) (2014) 14413–14419.

[27] A.K. Singh, T.C. Goel, R.G. Mendiratta, O.P. Thakur, C. Prakash, Dielectric properties of Mn-substituted Ni–Zn ferrites, J. Appl. Phys. 91 (10) (2002) 6626.

[28] S. Dabagh, K. Chaudhary, Z. Haider, J. Ali, Effect of sintering on Di-electric characteristics of AL-Cu doped cobalt ferrite nanoparticles, J. Nanosci. Nanotech. 19 (7) (2019) 4142–4146.

[29] D. Bouokkeze, J. Massoudi, W.H. Zez, M. Smari, A. Bougoffa, K. Khirouni, A. Bessais, Investigation of structural, optical, elastic and electrical properties of spinbel LiZn2Fe3O8 nanoparticles annealed at two distinct temperatures, RSC Adv. 9 (2019) 40940–40955.

[30] K.V. Chanderkar, K.M. Kant, Size-strain analysis and elastic properties of $CoFe_2O_4$ nanoplatelets by hydrothermal method, J. Mol. Struct. 1154 (2018) 418–427.

[31] M.P. Ghosh, S. Mukherjee, Microstructural, magnetic and hyperfine characterizations of Cu doped cobalt ferrite nanoparticles, J. Am. Ceram. Soc. 102 (2019) 7509–7520.

[32] M.M. Wu, L. Wen, B.Y. Tang, L.M. Peng, W.J. Ding, First principle study of elastic and electronic properties of MgZn2 and SeZn2 phases in Mg-Se-Zn alloy, J. Alloy Compd. 506 (2010) 412–417.

[33] K.B. Modi, Elastic moduli determination through IR spectroscopy for zinc substituted copper ferri-chromates, J. Mater. Sci. 39 (8) (2004) 2887–2890.

[34] Y. Pan, W.M. Guan, Probing the balance between ductility and strength: transition metal silicides, Phys. Chem. Chem. Phys. 19 (29) (2017) 19427–19433.

[35] S.A.B.I.N. Frantsevich, F.F. Varonov, Elastic constants and elastic moduli of metals and insulators Handbook, IN. Frant, Naukova Dumka, Kiev, 1983.

[36] M.A. Islam, A.K.M. Akther Hossain, M.Z. Ahsan, M.A.A. Bally, M.S. Ullah, S. M. Hoque, F.A. Khan, Structural characteristics, cation distribution and elastic properties of Cr^{3+} substituted stoichiometric and non-stoichiometric cobalt ferrites, RSC Adv. 12 (2022) 8502.

[37] M.R. Patil, M.K. Rendale, S.N. Mathod, R.B. Pujar, FTIR spectra and elastic properties of Cd substituted Ni-Zn ferrites, Int. J. Self-Prop. High Temp. Syn. 26 (2017) 33–39.

[38] A. Franco Jr., E.C.D. Lima, M.A. Noval, P. Well Jr., Synthesis of nanoparticles of $Co_xFe_{(3-x)}O_4$ by combustion reaction method, J. Magn. Magn. Matr. 308 (2007) 198.

[39] A.C.F.M. Costa, E. Tortella, M.R. Mavelli, R.H.G.A. Kiminami, Synthesis, microstructure and magnetic properties of Ni–Zn ferrites, J. Magn. Magn. Matr. 256 (2003) 174.

[40] A. Samavati, M.K. Mustafa, A.F. Ismail, M. Othman, M.A. Rahman, Copper substituted cobalt ferrite nanoparticles: structural, optical and antibacterial properties, Mater. Exp. 6 (2016) 475–482.

[41] N. Dhanda, P. Thakur, R. Kumar, T. Fatima, S. Hameed, Y. Slimani, An-Cheng Aidan Sun, Atul Thakur, Green-synthesis of Ni-Co nanoferrites using aloe vera extract: Structural, optical, magnetic, and antimicrobial studies, Appl. Organomet. Chem. (2023), https://doi.org/10.1002/aoc.7110.

[42] V.S. Kirankumar, S. Sumathi, Copper and cerium co-doped cobalt ferrite nanoparticles: structural, morphological, optical, magnetic and photocatalytic properties, Environ. Sci. Poll. Res. 26 (2019) 19189–19206.

[43] M.M. El-Masry, A. El-Razed Mahmoud, H.Y. Morshidy, R. Samadan, Cu2+ and Zn2 + doped cobalt spinel ferrite: insights on structural, thermal conduction, electric, magnetic and elastic properties, J. Mater. Sci.: Mater. Electron. 34 (2023) 383.

[44] N. Dhanda, P. Thakur, A.C.A. Sun, A. Thakur, Structural, optical and magnetic properties along with antifungal activity of Ag-doped Ni-Co nanoferrites synthesized by eco-friendly route, J. Magn. Magn. Matr. 572 (2023), 170598.

[45] K.M. Batoo, M. Hadi, R. Verma, A. Chauhan, R. Kumar, M. Singh, O.M. Aldossary, Improved microwave absorption and EMI shielding properties of Ba-doped Co-Zn Ferrite, Ceram. Int. 48 (2022) 3328–3343.

[46] D. Chahar, P. Thakur, A.C. Sun, et al., Investigation of structural, electrical and magnetic properties of nickel substituted Co–Zn nanoferrites, J. Mater. Sci: Mater Electron 34 (2023) 901, https://doi.org/10.1007/s10854-023-10273-5.

[47] P. Coppola, F.G. da Silva, G. Gomide, F.L.O. Paula, A.F.C. Campos, R. Perzynski, C. Kern, J. Depeyrot, R. Aquino, Hydrothermal synthesis of mixed zinc-cobalt ferrite nanoparticles: structural and magnetic properties, J. Nanopart. Res. 18 (5) (2016).